Characteristics of large Martian dust devils using Mars Odyssey Thermal Emission Imaging System visual and infrared images

Characteristics of large Martian dust devils using Mars Odyssey Thermal Emission Imaging System Visual and Infrared images.

M.C. Towner (1)*

(1) Planetary and Space Sciences Research Institute, Open University, Walton Hall, Milton Keynes, MK7 6AA, UK

Index terms:

3314 Atmospheric Processes: Convective processes

5405 Planetary Sciences: Solid Surface Planets: Atmospheres

5445 Planetary Sciences: Solid Surface Planets: Meteorology

6225 Planetary Sciences: Solar System Objects: Mars

6213 Planetary Sciences: Solar System Objects: Dust

*Corresponding author

Abstract

A search for martian dust devils has been carried out, using Mars Odyssey Thermal Emission Imaging System (THEMIS) visible-wavelength images. Simultaneous THEMIS thermal infrared wavelength images were then processed and analyzed, to investigate the thermal properties of the dust devils observed. 3079 images were checked, concentrating on northern spring, summer and autumn (L_S from 0° to 270°, 20°S to 50°N). Mars Express High Resolution Stereo Camera, Mars Global Surveyor Mars Orbiter Camera and other THEMIS visible images were used for comparison to potentially rule out any ambiguous geological features. Eight clear examples of dust devils have been found in five separate images, with a comparable number of unconfirmed possible devils. The rarity of dust devils observed is believed to result from a combination of the difficulty in identifying dust devils in medium resolution THEMIS data, and that the Mars Odyssey orbit flyover local time is later in the afternoon than would be optimum for dust devil searching. The temporal distribution of dust devil activity appears to be weighted more towards later afternoon, compared to Earth, but this may be a sampling effect due to size variation with time of sol, greater coverage later in the sol, or the small-number statistics. The thermal infrared images indicate that the lofted dust in the column is cooler than the surrounding surface, and must be equilibrating with the atmosphere in the dust devil. This energy transfer is estimated to be about 10% of the heat flux energy that is available to drive the systems. The ground shadowed by the dust column also appears colder than the surroundings, due to reduced solar illumination. From the visible-wavelength images, the shadows of the dust columns were used to estimate the column opacity, which in turn gave estimates of the dust loadings, which ranged from 1.9×10^{-5} to 1.5×10^{-4} kg m^{-3},

similar to lander-based observations. No thermal or visible trails are associated with the dust devils, indicating that the surface equilibrates quickly after the devil has passed, and that track counting as a dust devil survey technique must underestimate dust devil populations and consequently dust loading calculations, confirming previous work.

1. Introduction

Early studies of arid environments have noted the presence of convective vortices and dust devils [*Baddeley*, 1860; *Flower*, 1936], and their formation and occurrence has been studied for many years [*Balme and Greeley*, 2006; *Fitzjarrald*, 1972; *Kaimal and Businger*, 1970; *Ryan and Carroll*, 1970; *Sinclair*, 1966; *Snow*, 1987]. Convective vortices are symptomatic of atmospheric instability, requiring strong insolation to form [*Ryan and Carroll*, 1970; *Ryan*, 1972]. They have a low pressure, hot core, and a tangential wind gradient, and if powerful enough they are capable of entraining surface material and becoming dust devils. Terrestrial dust devil investigations have taken on a new interest relatively recently, primarily due to the observations of dust devils on Mars.

Dust devils appear to be a ubiquitous process on Mars, having been visually observed by the Viking Orbiters [*Thomas and Gierasch*, 1985], Mars Global Surveyor [*Cantor et al.*, 2001; *Malin and Edgett*, 2001], Mars Odyssey [*Cushing et al.*, 2005], Mars Express [*Stanzel et al.*, 2006; *Stanzel et al.*, 2008], and the landers Mars Pathfinder [*Metzger et al.*, 1999] and the Mars Exploration Rovers [*Greeley et al.*, 2004]. Currently, the surface boundary layer wind speeds on Mars are considered borderline to be sufficient to initially loft fine dust particles into the atmosphere [*Greeley and Iversen*, 1985], therefore particle lofting by impact saltation, including dust devil action, has been posited as one of the main mechanisms for moving and redistributing dust on Mars.

Consequently, they may be potentially hazardous to both robotic and manned missions to Mars. Terrestrial studies also indicate their potential to degrade the air quality, and occasionally damage light aircraft [*Hess and Spillane*, 1990].

Dust devils on Mars are believed to form and to be influenced by identical factors to those on Earth [*Renno et al.*, 1998], and detailed study of this hypothesis will enable terrestrial analogues and modeling to be successfully applied to Mars. Several diagnostic features such as size and temporal frequency statistics, and the detailed structure of the dust devil (the nature of temperature, wind and pressure changes within it) have been considered theoretically [*Renno et al.*, 1998] and directly compared between Mars and Earth (see [*Balme and Greeley*, 2006; *Cantor et al.*, 2006] and references therein for a review). A dust devil is special case of a convective vortex, and one meteorological diagnostic of a convective vortex is the presence of a hot core [*Fitzjarrald*, 1973; *Ives*, 1947; *Kaimal and Businger*, 1970; *Ringrose et al.*, 2003; *Sinclair*, 1964; 1973; *Tratt et al.*, 2003]. Data from the Mars Odyssey Thermal Emission Imaging System (THEMIS) offers the opportunity to provide insight into this structure from orbit, as this instrument observes simultaneously in visible wavelengths and in the thermal infrared. This provides the potential to extract the dust devil's core temperature, provided the core is large enough to be clearly resolved (i.e. greater than 100 m across). To investigate this, a targeted survey for dust devils on Mars was performed, intended to capture well-observed exceptionally large dust devils.

The statistics generated while searching for dust devils using THEMIS also help to address the issue of dust devil activity as a function of time of day; THEMIS is well

86 suited to this type of activity, as the instrument has moderate resolution and large
87 coverage. The THEMIS instrument is summarized in [*Christensen et al.*, 2004]).

88 On Earth, dust devils usually form in dry areas, such as deserts, on sunny days in
89 spring or summer [*Cooley*, 1971]. Surface heating is needed, but the atmospheric thermal
90 gradient (driven by the ground-air temperature difference) is more important than
91 absolute high temperatures, as dust devils have been recorded in sub-arctic climate where
92 the air temperature was about 18°C [*Grant*, 1949]. Most terrestrial dust devils are less
93 than 150 m tall and last only a few minutes, with exceptional observations of dust devils
94 up to a few thousand meters in height lasting up to an hour [*Ives*, 1947].

95 On Mars, similar formation criteria are expected, but due to the different
96 atmospheric environment (e.g. a larger boundary layer, and smaller Grashof number,
97 [*Fuerstenau*, 2006]), they tend to be larger. It is possible that the generally lower thermal
98 inertia of the martian surface means that it responds faster than the Earth to insolation
99 changes, which in turn implies that dust devils may begin to form earlier than on Earth,
100 and peak during midday to early afternoon. This appears to be supported by the limited
101 number of lander observations; *Ringrose et al.* [2003] discussed convective vortices at the
102 Viking Lander 2 site as early as 10 am, with a relatively flat temporal distribution, while
103 Mars Pathfinder data [*Murphy and Nelli*, 2002] shows a peak vortex rate at midday.
104 However, these meteorological instruments are measuring convective vortices, and
105 inferring the presence of true dust devils, so caution must be taken in comparing them to
106 visual observations of dust devils. On the Earth, the temporal distribution of dust devils
107 shows a distinct skew towards the afternoon [*Sinclair*, 1969]. THEMIS data can also help
108 to determine this temporal distribution on Mars, as it has a different local time of day

109 flyover to earlier orbital surveys [*Cantor et al.*, 2006; *Fisher et al.*, 2005]. A clear
110 observation of a dust devil in THEMIS will simultaneously quantify dust devil
111 dimensions, dust loading, and temperatures allowing comparison with terrestrial work.

112 *2. Previous martian studies*

113 On Earth, the larger dust devils are approximately 50-100 m in diameter and over a
114 kilometer high [*Balme and Greeley*, 2006; *Bell*, 1967]. These are small compared to
115 Mars, where dust devils have been observed that are over 1 km across and up to 10 km
116 high [*Fisher et al.*, 2005; *Thomas and Gierasch*, 1985]. Tracks left by the passage of dust
117 devils leave behind appear to be ubiquitous across Mars, and active vortices have been
118 recorded in data from almost all Mars missions, including landers equipped with
119 meteorology instrumentation or suitable imaging sensors. The two Viking Landers
120 detected vortices in the late 1970s by their meteorological signal [*Ryan and Lucich*,
121 1983]. Ryan and Lucich's analysis has shown that the Viking Landers appeared to
122 encounter about 0.6 dust devils per sol, as compared to the 2 dust devils per sol found in
123 the Pathfinder data [*Murphy and Nelli*, 2002; *Ringrose et al.*, 2003].

124 In 1999, the Mars Pathfinder lander took images in which five different dust devils
125 were ultimately identified [*Metzger et al.*, 1999], although *Ferri et al.* [2003] has
126 expanded upon this number. More recent orbital images acquired by the Mars Global
127 Surveyor Mars Orbiter Camera (MOC) detected many dust devils, allowing detailed
128 viewing and statistics to be generated [*Cantor et al.*, 2006; *Fisher et al.*, 2005]. Estimates
129 of dust devil movement traverse velocity have been made by Mars Express High
130 Resolution Stereo Camera (HRSC) [*Stanzel et al.*, 2006], giving speeds on the order of
131 20 ms^{-1}. Mars Reconnaissance Orbiter has imaged dust devils at pixel resolutions of

about 6 m, (using the High Resolution Imaging Science Experiment, HiRISE), and at 20 m, (using the Context Camera, CTX), as noted on the mission web page but not as yet formally published. Dust devils appear to be very common on Mars: Thomas and Gierasch [1985] identified almost 100 dust devils in Acidalia Planitia in the Viking Orbiter images, although resolution limitations may have obscured the smaller dust devils. Additionally they appear to often leave tracks behind them on the martian surface [*Edgett and Malin*, 2000], at nearly all latitudes [*Balme et al.*, 2003b; *Cantor and Edgett*, 2002; *Whelley and Greeley*, 2006].

Of most interest to this study is the recent publication by [*Cushing et al.*, 2005], which reports the first detection of a dust devil in both THEMIS visible and infrared (and the only detection by THEMIS published to date). This particular dust devil had a diameter of approximately 375 m, but is only weakly visible in the infrared data. Intriguingly, it was detected at an altitude of more than 16 km above the Mars datum, where the atmospheric pressure is very low (about 1 mbar), and also occurred relatively late during the day (a local time of 16:06).

3. Approach

3.1 The THEMIS Instrument

The THEMIS Instrument is comprised of two parallel systems; a thermal infrared (IR) emission imager and a visible-wavelength imager [*Christensen et al.*, 2004]. Visible-wavelength images have resolutions of 18, 36 or 72 m/pixel, compared to the infrared at about 100 m/pixel. The two parallel multi-spectral systems operate independently, and can be used to observe the same target simultaneously. Standard radiometrically

154 calibrated images from the THEMIS dataset can be obtained from the public domain
155 NASA Planetary Data System (PDS) online archive.

156 The visible-wavelength imager can observe in five bands, but typically only band 3
157 is used (centered at 654 nm). The infrared imager can observe ten bands, between
158 6.78 μm and 14.88 μm, with each differing in its ability to highlight different surface (or
159 atmospheric) features [*Christensen et al.*, 2004]. IR bands 3 (7.93 μm) and 5 (9.35 μm)
160 are believed to have the best contrast for detection of surface dust movement and
161 transient features, based on spectral modeling work and previous observations of
162 suspended dust [*Cushing et al.*, 2005; *Smith et al.*, 2003]. As noted by [*Brumby et al.*,
163 2003], band 3 is mostly insensitive to water and the atmosphere, and can be used for a
164 good visualization of the ground surface, while the appearance of dust is enhanced in IR
165 band 5 (due to the atmospheric dust strongly absorbing photons at 9.35 μm). Using
166 Stephan's law (assuming a fixed surface emissivity and a transparent atmosphere) and the
167 infrared data, a brightness temperature image of the surface (in Kelvin) can be
168 constructed; this is provided as a derived data product on the NASA PDS for each
169 infrared image.

170 ### *3.2 Image selection and treatment*

171 Considering the resolution of THEMIS IR observations, it is clear that directly
172 detecting medium size (a few 100 m) dust devils would not be easy. Hence we decided to
173 look initially in the higher resolution visible-wavelength imagery, and then compare to
174 the infrared, whilst using other observations from THEMIS and other missions to rule out
175 permanent or ambiguous geological features. This technique is supported by the results of
176 [*Cushing et al.*, 2005] where the dust devil seen has a diameter of 375 m, and is clearly

177 resolved in the visible-wavelength data, but shows only a minor deviation from surface
178 emissivity in the infrared image.

179 We decided that a semi-targeted search of particular regions was likely to be the
180 most successful approach. The criteria for targeting consideration were based on two
181 questions; 'will there be dust devils there, and will they be observable in the visible and
182 the infrared data?' As such, 'borderline' dust devil producing areas, which might lack the
183 required atmospheric instability and only produce a few dust devils (and hence very few
184 exceptionally large dust devils) were not included [*Ryan and Carroll*, 1970]. The search
185 therefore focused on areas previously noted as major dust devil producing areas with
186 large dust devils observed, for example the Amazonis region [*Cantor et al.*, 2002; *Cantor*
187 *et al.*, 2006; *Fisher et al.*, 2005]. The study region should also be close to the equator, as
188 this is where conditions are most suitable for dust devil formation [*Biener et al.*, 2002].
189 However it is also important to consider a large enough percentage of the martian surface
190 in order to give a reasonable chance of success and to produce statistically meaningful
191 results.

192 With this in mind, a latitude range of 20°S to 50°N was selected, over the full
193 longitude range, which favors warm areas and maximum levels of light per sol.
194 (Although dust devil tracks are generally seen to be maximum in the 40-60 latitude bands
195 [*Balme et al.*, 2003a; *Whelley and Greeley*, 2006], they are seen at all lower latitudes.)
196 Dust devil activity is highest in the spring and summer, so images acquired between solar
197 longitude (L_s) 0° to 270° (northern spring, summer and autumn) were used. Obviously
198 dust devils will not occur at night, and the largest are expected to occur during the

199 brightest daylight hours, so only images acquired between local times of 11:00 to 16:30
200 were considered.

201 These constraints were applied to a search of the NASA PDS, and images were
202 retrieved from the PDS and analyzed systematically at increasing magnification,
203 investigating and recording features of interest at greater detail as required. Potential
204 candidates were identified initially based on the criteria of just the presence of a dust
205 cloud like object. These candidates were then compared with images of the same regions
206 taken by HRSC, MOC, Mars Reconnaissance CTX, or other THEMIS data to confirm the
207 presence of a dust devil (dust devils are transient features, and should not appear in other
208 images of the same location acquired at different times). In a small number of cases, there
209 were no comparable images. Those candidates were discarded from the list of confirmed
210 dust devils, but are considered separately later. Rejection was based on a judgment that
211 these particular anomalies were ambiguous – the features lacked a clear shadow, or a
212 clear track/trail, and lacked structure indicating a dust column; if they were dust related,
213 rather than geomorphological, then they were most likely dust flurries or fronts, lacking
214 convective vorticity.

215 The visible representations of confirmed dust devils were then analyzed in detail;
216 where possible the height of the dust devil was calculated using the shadow projection
217 and the Solar Incidence angle (from the PDS label). Diameter was directly measured
218 from the image.

219 Simultaneous observations through the THEMIS infrared system provide a derived
220 brightness temperature record (BTR) of the same locale. These data give local

221 temperatures of the ground and dust devil, providing additional information on dust devil
222 structure.

223 *4. Results and discussion*

224 *4.1 Survey results*

225 The PDS search generated 3079 images within the region of interest, from 2002-04-
226 18 to 2006-03-03, from THEMIS datasets release_id 0001 to 0017 (the latest release at
227 the time of beginning this work). In reality, observations taken earlier than 16:00 local
228 time are only from the orbit phasing part of the mission, early in the spacecraft lifetime,
229 and there are none after 2002-07-20. Observations with a local time from 16:00 to 16:30
230 are available throughout the mission. Initial analysis revealed 294 candidate images that
231 warranted further investigation. Comparison of coexistent images from a variety of
232 sources as discussed allowed removal of false positives by eliminating features that have
233 not moved between images. Overall, only eight dust devils were reliably detected from
234 five image frames (there are two frames which each have multiple dust devils). The
235 locations of these are shown in Figure 1, and summarized in Table 1. Figure 2 gives
236 detailed images of the dust devils detected, showing both the visible data, and the IR
237 thermal results (discussed later). Due to the conservative approach taken to eliminating
238 false positives, the numbers of dust devils confirmed here probably represents a lower
239 bound, highlighting the clearest, most apparent events, with ambiguous or smaller events
240 excluded. Events that were eventually unconfirmed as dust devils, primarily to a lack of
241 supporting overlapping images are shown in Table 2, and examples of these are shown in
242 Figure 3. These are discussed in more detail later.

<fig 1 here>

<table 1 here>

<fig 2 here>

<table 2 here>

<fig 3 here>

<table 3 here>

Only a few active dust devils were detected by THEMIS in this work, suggesting that these detections are of relatively rare exceptional events, requiring a fortuitous combination of size and time of day. No trend is seen with altitude above the Mars datum. In Figure 2, dust devils 5, 6 and 7, appear more ambiguous, and it is possible they are in fact dust fronts or flurries, due to the apparent lack of structure. Dust devils 5 and 6 have no clear shadow, so no estimate of height could be made. This ambiguity is somewhat supported by dust devil 7, as close examination of the shadow cast, which although distinct, appears to indicates a lower height than might be expected. It may be that the dust loading is lower later in the day, possibly due to the effect of the time of day itself (a less intense dust devil due to lower illumination), or of course it may just be that these areas happen to have less available dust on the ground to loft. Table 3 summarizes the survey statistics obtained from this search. From this and the PDS image local time statistics, there is a clear observational bias due to the mean flyover time of Mars Odyssey, of about 16:30, such that there are relatively few images to search before 15:30,

and none before 15:00, when dust devil activity is observed to be higher [*Cantor et al.*, 2006; *Christensen et al.*, 2004].

Statistically, it would seem that very few dust devils have been found. As noted by *Fisher et al.,* [2005], very few dust devils occur in the late afternoon on Mars, in contrast to the Earth. The survey of *Cantor et al.,* [2006] using MOC found dust devils in 0.4% of the images studied, far greater than observed here (MOC over-flight is at about 14:00 local time). For example, peak rates seen during northern spring in the Syria-Claritas region by [*Cantor et al.*, 2006] were about 1.4×10^{-3} dust devils km^{-2}, observed between 14:00 and 15:00. [*Fisher et al.*, 2005] find very similar peak values for Amazonis Planitia, again using MGS MOC data. One possibility is that the lack of dust devils later in the day is driven by the low surface thermal inertia and the thin atmosphere both loosing heat very quickly once the Sun is past zenith, resulting in less energy to drive the process. Of the 498 dust devils seen by Spirit, [*Greeley et al.*, 2006], only two are after 15:30, but there may be some sampling effect due to the observing constraints of the rover, which is permitted to produce more images during the middle of day. When studying terrestrial dust devils in the southwestern USA, *Sinclair,* [1969] had noted a tendency for larger dust devils to appear later during the day; one might expect this to be applicable to Mars, and this would be consistent with the rate distribution shown in Table 3 above. *Greeley et al.,* [2006] detect no trend of diameter with time of day.

For comparison, the biggest dust devil seen by Spirit is about 280 m [*Greeley et al.*, 2006]. The survey conducted by *Fisher et al.,* [2005] (using MGS MOC Wide Angle images) detected even larger examples, with the largest being about 8.5 km high and about 500 m in diameter.

288 This survey concentrated on detecting large well-resolved dust devils that could be
289 visible in the infrared; as such some smaller candidates (that may have been real) were
290 discarded, as they lacked clear diagnostic features (shadow, track etc). This may skew the
291 perceived detection rate. Ultimately the smallest resolvable is 4-8 pixels in the visible
292 (approximately 80-160 m), but any dust devils this small will have very little expression
293 in the lower resolution THEMIS IR image. Table 2 lists dust devil candidates that were
294 ultimately rejected or remain unconfirmed. The majority are rejected purely on the basis
295 of size and image resolution; usually there is one single observation that is just not clear
296 enough to be useful. Figure 3a gives an example of this. In a few cases, signal to noise is
297 insufficient to resolve the candidate clearly against the background structure. Figure 3b
298 shows an example of such a candidate, where there may be changes between the two
299 images, but image saturation prevents confidence that this is a dust devil. Future data
300 releases giving increased coverage may help to clarify the status of some of these
301 candidates. Due to the small numbers of dust devils confirmed, statistics derived from
302 this study are sensitive to the rate of the largest dust devils, and one must be careful in
303 over interpreting such small number statistics.

304 A further consideration is that later afternoon dust devils have been suggested to be
305 less intense and ordered, and more flurry-like [S. M. Metzger, pers. comm., 2005].
306 Laboratory investigations by *Church et al.,* [1979] and *Mullen and Maxworthy,* [1977]
307 related the compactness of the structure of tornado-like vortices formed to a 'swirl ratio',
308 which compares horizontal to vertical momentum. The swirl ratio will evolve throughout
309 the day, via the atmospheric stability and average wind speeds, so one would expect a
310 variation in dust devil compactness through the day. Terrestrially this is demonstrated by

311 considering in Figure 4, where two extremes are presented. One should expect the same
312 variation on Mars, as the underlying mechanism for dust devil formation on the two
313 planets are probably very similar [*Renno et al.*, 1998; *Renno et al.*, 2000].
314
315 <fig 4 here>
316
317 It should be noted that none of dust devils found here have produced visible tracks.
318 This implies that track-counting alone cannot produce accurate population statistics. This
319 has also been noted by *Cantor et al.,* [2006].
320 The dust devil observed by *Cushing et al.,* [2005] on Arsia Mons is not captured by
321 this survey: It is within the proscribed latitude range (9.38°S), and local time of day
322 (16:06), but occurred at L_s=341, and as such it could be considered a 'southern' dust
323 devil, occurring in southern summer. It would be detected if this survey was repeated
324 with a southern hemisphere orientation. This might be worthwhile, given that the data of
325 *Whelley and Greeley,* [2006] indicated that the southern hemisphere has more visible dust
326 devil tracks than the northern during peak seasons, per unit area. (see also [*Cantor et al.*,
327 2006]). The Cushing dust devil appears similar in appearance to the later dust devils seen
328 here, with little or no expression in the infrared temperature data. However infrared
329 absorption is weakly seen for this devil in THEMIS band 5, indicating the presence of
330 suspended dust [*Smith et al.*, 2003]. There is clearly no question that the Arsia Mons
331 feature is a dust devil, given its structure: It has a well defined shadow and height,
332 ([*Cushing et al.*, 2005], fig 2), whereas the features here suspected to be gusts do not. The
333 high altitude at this point means that the atmosphere is thin, with a low dust loading, and

hence a low dust opacity. This would have acted to increase the apparent contrast in the IR band 5 and the brightness temperature data; however no temperature excursion is seen. If this structure and temperature difference is typical for this size of dust devils, then it implies that circumstances may have to be exceptionally fortunate at lower altitude for thermal anomalies to be observed, and so in some cases dust devil core temperatures may be difficult to extract from dust devil events seen in THEMIS data.

4.2 Infrared Temperature Data results

Figure 2, right hand column shows the derived temperature anomalies associated with the dust devils. The visible-wavelength image brightness is overlain as contour lines, while the color pixels are used to represent temperature data. In all images, the temperature pixels are 100 m across.

The suspended fine dust in the devil column (about 2-3 μm diameter, [*Tomasko et al.*, 1999]) will appear clearest in IR band 5 [*Smith et al.*, 2003], because suspended particles of this size interact with the incoming sunlight with wavelengths near to 9 μm. Band 3 is less sensitive to suspended dust, and observes the ground below the dust devil. As such, a comparison of IR data from bands 3 and 5 can be used as a check for the presence of lofted dust. The temperature data are derived from band 5, and so give the temperature of the dust devil dust cloud (or the dusty surface if the atmosphere is clear).

Dust devil 2 (Figure 2b) has the clearest classic dust devil structure. The temperature data shows clear evidence of the shadow cooling the ground, and of the lofted dust being cooler than the surface. However, although the core should be about 3-4 pixels across, it is not immediately obvious as an expected ‘hot spot’, instead appearing cold. This is even more apparent in dust devil 3 (Figure 2c), where the shadowed surface

357 is only slightly cooler than ambient, but the relatively weak visible dust plume slightly to
358 the SW of the main core appears strongly-cooled in the temperature data. From previous
359 terrestrial and martian meteorological work it is known that dust devils have a hot core,
360 due to their convective nature, but on Earth the core is generally dust free above the
361 saltation skirt [*Ryan and Lucich*, 1983; *Sinclair*, 1969], and as such would not be
362 observed by the dust sensitive THEMIS infrared data. These observations are consistent
363 with the suspended dust appearing cold relative to the hot surface, possibly due to the loss
364 of heat into the dust devil air column. In a terrestrial context, *Sinclair,* [1966] discusses
365 modeling to consider the heat flow from the relatively hot dust picked up into the
366 surrounding air within the column, which would then act to heat the air column (and cool
367 the dust). *Fuerstenau,* [2006] indicated that the solar warming of the suspended dust
368 grains is a major component of the thermodynamics of dust devils, as these warmed
369 grains will transfer heat into the atmosphere. This warming will be strongest on the edges
370 of the dust column (dependent on the opacity), which may then result in the inner dust
371 being shaded somewhat, and thus relatively cooler. It would appear that if this warming is
372 occurring then the warmed outer layers are relatively thin, and THEMIS is observing the
373 cooler-than-ambient inner layers of dust.

374 From the thermal data in Figure 2, the lofted dust column is about 1 K cooler than
375 the surface in all cases. Given that the system is roughly in a steady state, and taking
376 plausible values for the dust loading (derived in the following section), and using the
377 specific heat capacity of basalt for the dust (840 J/kg-K, [*Roberts-Austen and Rücker*,
378 1891]), this temperature drop results in about 100 W/m^2 of heat loss from the dust, as
379 once lofted the dust immediately and isometrically re-radiates this absorbed heat. This

compares to the total energy available to drive dust devil activity of about 430 W/m^2 from the later afternoon Sun on Mars. Because nearly 25% of the incoming insolation energy is dissipated by this process, the presence of the dust should be taken into account when modelling dust devils [*Fuerstenau*, 2006; *Sinclair*, 1966].

In reality, orbital instruments are unlikely to ever be able to see right down the dust-free core of the dust devil, since dust devils are not precisely vertical, but tend to show a tilt in the direction of ambient wind. A ring of slightly cooler air surrounding the dusty core has been reported previously in some cases [*Ives*, 1947; *Ringrose et al.*, 2003] (although this is somewhat tentative [*Balme and Greeley*, 2006]), but the resolution here is insufficient to confirm this.

Dust devils 4 and 7 show no significant temperature anomalies, and so is possible that they may not be thermally driven, but might instead be wind gusts capable of lofting dust but lacking convective vorticity, similar to very small local fronts or storms [*Briggs et al.*, 1979]. However, such storms generally lack the column-like structure seen here, and are larger, so it is more plausible that the temperature anomalies are merely not large enough to be detected by the instrument, or that the upper-dust-column temperatures are equilibrating with surface temperatures, effectively shielding any temperature anomalies closer to the ground. The contour data clearly shows that dust devil 7 has a apparent double brightness peak, and this may be a compound dust devil, made up of two (or more) vortices circling each other; such structures are relatively common terrestrially in less well defined dust devils such as Figure 4(b) [*Balme and Greeley*, 2006].

There are weak hints of a hot anomaly seen on the ground in immediate sunward direction of dust devil column in dust devils 1, 2, 3, and 6 (Figure 2), which could be a

result of the dust column absorbing sunlight and scattering light onto the surrounding surface, which is adding to the direct solar illumination of this area of the surface. These apparent anomalies are very weak, and near to the resolution of the instrument, so further work is required to confirm this effect. In the case of dust devil 2 it is just plausible that this weak hot anomaly may be a false positive caused by the existing apparent temperature patterns in the surrounding surface. On Mars one would expect these anomalies to be a weak effect, given the dust devil opacity, but it might be possible to further investigate these phenomena in terrestrial dust devils using appropriate instrumentation [*Lorenz*, 2004].

In no case does there appear to be any apparent cold (or hot) trail on the ground upwind of the dust devil, marking the passage of the dust devil. Either the heat being removed from the ground by the dust devil is below the resolution of the instrument, or the ground is equilibrating quickly, which might be expected due to the low thermal inertia of the dusty surface layer.

4.3 Opacity and dust loading from consideration of shadowing

A significant shadow is seen alongside most observed dust devils. Hence, it is clear that the dust devils have significant opacity, and the depth of this shadow can be used to approximate the dust loading. We summarize the technique here, for a more detailed description of the method, see *Fuerstenau,* [2006]. We assume a Lambertian surface with constant albedo and geometric properties, and that the drop in illumination caused by a dust devil's shadow is not influenced by surface variations (Figure 5). By quantifying this amount of light lost, it is possible to estimate column absorption along the line of illumination. The measured dust devil diameter combined with the sun altitude above the

426 horizon allows opacity to be derived, which can then be related to atmospheric dust
427 loading using previous work ([*Landis*, 1996], [*Metzger et al.*, 1999]).

428

429 <fig 5 here>

430

431 Considering the schematic of a dust devil in Figure 5 the average radiances of the
432 dust devil and surface (R_{dd} and R_s respectively) can be extracted from image data of the
433 dust devil shadow and adjacent areas outside the shadow. As measured by THEMIS,
434 these are both relative radiances, but both are linearly related to absolute radiance by the
435 same factor, which cancels out when R_{dd} and R_s are ratioed. To compensate for variations
436 in terrain reflectivity between areas with and without shadows, a separate THEMIS image
437 of the scene (with dust opacity and viewing geometry as similar as possible to the dust
438 devil image) was considered. Radiance values from areas of the second image
439 corresponding to the previously defined dust devil shadow and well illuminated terrain
440 are used to derive *r*, the compensating ratio of the reflectances of the two areas.
441 Additionally, one must account for the relative amounts of direct and diffuse illumination
442 because at least some of the radiance emitted from the dust devil's shadow is probably
443 due to scattered light from the sky and other features [*Fuerstenau*, 2006]. To evaluate the
444 effect of the diffuse illumination, a nearby area of terrain shadow (only illuminated by
445 diffuse lighting) is considered. The pixel values from this terrain shadow are then
446 subtracted from the dust devil shadow's pixel values. For this opacity calculation, byte-
447 scaled pixel units are used, for convenience. All measurements needed to calculate
448 opacity are relative, and from the same image, so byte-scaling of the absolute radiances

449 cancels out. This canceling can be shown from Equation 1 using simple algebra: Replace
450 all terms of R (the byte-scaled radiances) with a linear scaling such as A_1x+A_0, where A_1
451 and A_0 are constants, and x is the original, non-byte-scaled, radiance (in $Wcm^{-2}Sr^{-1}\mu m^{-1}$);
452 after simple manipulation, A_1 and A_0 completely cancel out and disappear from the
453 equation, provided all radiances come from the same image. However, the THEMIS data
454 files from the PDS must be the radiometrically calibrated format (RDR), rather than the
455 raw data, to account for instrumentation effects such as non-linear sensitivity and varying
456 zero offset. Additionally, the brightly-lit dust devil column itself could act as a secondary
457 illumination source, acting to apparently brighten the shadow. Such an effect would be
458 small, due to the relatively low opacity of the dust devil (and hence the low ratio of
459 scattered to direct light), and computationally difficult to deal with, and is neglected here.
460 It would have the effect of making the shadow appear brighter, such that the dust loading
461 of the devil would appear lower than reality.

462 From Figure 5, the ratio of the radiances is then approximately

463

$$\frac{r(R_{dd}-R_T)}{(R_s-R_T)}=\frac{I_{src}e^{-\tau}}{I_{src}}=e^{-\tau} \qquad \textbf{(Equation 1)}$$

464

465 Where τ is the opacity, R_T is the diffusely lit terrain, and I_{src} is the source intensity
466 (which is unknown, but cancels out). From *Landis,* [1996], who considered martian dust
467 opacity with reference to solar panel loading, the opacity can be related to the number
468 density of particles in the air by

469

$$\tau = QAN_O \quad \textbf{(Equation 2)}$$

Where Q is the scattering efficiency, A is the particle average cross sectional area, and N_o is the column number density. Due to the geometry of the situation, the path length measured is the dust devil diameter with a factor of the sine of the solar illumination angle, θ (A vertical dust column is assumed), so the number density, n, becomes

$$n = \frac{N_O}{D \sin\theta} \quad \textbf{(Equation 3)}$$

Where D is the dust devil diameter, giving

$$n = \frac{\tau}{QA_O D \sin\theta} \quad \textbf{(Equation 4)}$$

Q is taken as 2.98 at 600 nm [*Ockert-Bell et al.*, 1997], which is the closest wavelength data available to THEMIS visible band 3 (654 nm), as used for these observations. The lofted dust grain size distribution in a martian dust devil is not well known. The lower dust devil is assumed to be saltation dominated [*Greeley et al.*, 2003], so a mean grain diameter is taken as 75 μm, the size of the most easily saltated dust diameter on Mars [*Greeley and Iversen*, 1985]. Dust devils are believed to loft finer dust by a low pressure 'sucking' effect, as well as saltation [*Balme and Hagermann*, 2006;

488 *Greeley et al.*, 2003], but this is not yet well understood in detail. Qualitative modelling
489 implies that this effect should be strongest for small well-formed dust devils on the Earth,
490 as opposed to the targets of this work, large dust devils on Mars [*Balme and Hagermann*,
491 2006]. If significant, this excess dust lofting effect might result in a smaller average dust
492 grain size, by increasing numbers of smaller particles. *Landis,* [1996] assumed particle
493 diameters of 24 μm for his calculations, but he derived this value from the weighted mean
494 of the suspended dust in the full atmospheric column, as relevant to solar panel
495 obscuration. A factor of three difference in particle diameters is probably within the
496 intrinsic variability in dust loading seen in dust devils, as can be seen from dust loading
497 estimates from the Spirit rover ([*Greeley et al.*, 2006], discussed in following section).
498
499 <table 4 here>
500
501 Table 4 gives the physical parameters measured from the images, and the calculated
502 dust devil loading. For comparison, the Spirit rover in Gusev crater recorded values from
503 3.9×10^{-9} to 4.6×10^{-4} kgm^{-3}, with a mean of 2.07×10^{-5} kgm^{-3} [*Greeley et al.*, 2006], while
504 the estimated dust devil loading from Mars Pathfinder is 7×10^{-5} kgm^{-3} [*Metzger et al.*,
505 1999]. Our calculated values (derived from spacecraft observations) are reassuringly
506 similar to the values derived from lander observations. The dust concentration derived
507 here is similar to the values of *Greeley et al.,* [2006], but it is not possible to estimate a
508 dust flux, as there is no record of the vertical dust devil wind speed. However, the
509 concentrations and sizes are similar to those observed by Spirit [*Greeley et al.*, 2006], so
510 one might expect the flux to be comparable. The values for visible-dust opacity

511 measurements, from 0.06 to 0.23 across the width of the column (typically a few hundred
512 meters), are comparable to estimates of 0.03-0.40 for the full atmospheric column [*Smith*
513 *et al.*, 2000], which illustrates how much greater than the average dust loading the devil
514 dust loads are.

515 Although this approach is general, in the ideal it requires that the dust loading is
516 strong enough to make a clear dust-devil shadow and that there is a compensating image
517 (which should ideally be a THEMIS visible-wavelength image as well). The values for r
518 in Table 4 are all very close to 1, which highlights the fact that the dust devils are moving
519 across smooth plains, which have a low contrast. The inclusion of r in the calculations
520 would be more important if a dust devil was amongst terrain with a variety of albedos
521 which may have altered, such as on top of older dust devil streaks. In cases where no
522 THEMIS compensating image exists, Mars Express HRSC (the nadir observing channel)
523 could be used as a substitute, as this observes at 650 nm, compared to 654 nm for
524 THEMIS band 3. However this should be used with caution, as the flyover time of day
525 may be different, resulting in a different surface temperature and illumination angle: r
526 would also be altered by variations in atmospheric opacity, or any surface albedo changes
527 such as frost.

528 ## *5. Conclusions*

529 Because THEMIS observes simultaneously in both visible and thermal-infrared
530 wavelengths, it provides a unique dataset for studying dust devils, allowing simultaneous
531 analyses to be performed of both physical and thermal properties. To initially detect the
532 dust devils, a survey of THEMIS visible-wavelength images was conducted for L_s from
533 0° to 270° and latitude 20°S to 50°N, initially using THEMIS visible-wavelength

534 observations. 3079 images were searched manually, and then cross-referenced against
535 other images of the same areas to eliminate false positives. Eight dust devils in total have
536 been identified, in five images, ranging in diameter from 170 to 335 m.

537 The number of dust devils detected is approximately two orders of magnitude fewer
538 than were detected in previous studies [*Cantor et al.*, 2006; *Fisher et al.*, 2005]. This
539 discrepancy probably reflects the later flyover local time of Mars Odyssey (typically
540 16:30), coupled with the fact that the formation of dust devils may be more clustered
541 around midday on Mars than on Earth. Previous studies used Mars Global Surveyor data,
542 which has a local flyover time of around 14:00.

543 It appears likely that the late afternoon dust devils are more disordered in structure
544 than ones detected earlier in the afternoon, perhaps because of the weaker driving
545 insolation. It is possible (although unlikely given their structure) that the latest two dust
546 devils (numbers 6 and 7, Figure 2) seen are saltation capable wind gusts but lacking in
547 convective vorticity.

548 Using the calibrated surface radiances from the visible-wavelength imagery, and
549 observing the loss in radiance in the shadowed surface, we estimated that the dust loading
550 in the columns ranges from 1.94×10^{-5} to 1.53×10^{-4} kgm^{-3}, and are comparable to the
551 values derived from surface measurements for Mars Pathfinder and Spirit ([*Greeley et al.*,
552 2006; *Metzger et al.*, 1999]). The values here are derived from orbit, of the largest dust
553 devils, and yet the loadings are very similar to those from smaller lander-observed devils.
554 Measurements from orbit provide a more broadly applicable method for estimating dust
555 loading in martian dust devils than the spatially limited data acquired from landing craft
556 observations.

557 THEMIS also observed the dust devils at infrared wavelengths, as well as visible
558 wavelengths, and this infrared data can be used to derive surface temperature data. The
559 dust devils observed do not have a hot temperature anomaly, although the air temperature
560 in convective vortex cores has been shown to be higher [*Balme and Greeley*, 2006]. This
561 lack of a visible hot core is probably a shielding effect resulting from the dust column
562 blocking sight of the core, although THEMIS band 5 is primarily sensitive to dust, and
563 the core may be dust free. THEMIS infrared data indicates that the dust column is cooler
564 than the surrounding ground surface, implying that the dust has equilibrated with the
565 atmosphere after lofting. This loss of energy may be a significant part of the energy flow
566 of a dust devil [*Fuerstenau*, 2006; *Sinclair*, 1966]. There are also indications that the dust
567 column briefly shadows and cools a small portion of the surface.
568 Thermal tracks on the surface upwind of the dust devils are not detected by
569 THEMIS, indicating that the low-thermal-inertia surface equilibrates quickly after dust
570 devils pass (or that temperature drop is below the resolution of the instrument).
571 Additionally the dust devils discussed here did not produce visible tracks either,
572 suggesting that track counting statistics may not accurately represent dust devil
573 populations, as previously noted by *Cantor et al.,* [2006].
574 THEMIS 18-m visible-wavelength images can resolve most dust devils, but this is
575 not an perfectly suited instrument for broad surveying (mostly because of the late
576 observational times when most dust devils have expired). As more data released to the
577 NASA PDS, more dust devils that have been captured should be available, and searches
578 of the southern latitudes may be particularly promising, due to their high density of dust
579 devil tracks at some times of the year compared to the north [*Whelley and Greeley*, 2006].

580 Very recently Mars Odyssey has moved to an earlier orbit, which should also improve the
581 probability of observing dust devils. Dust devil orientated observations do require that
582 THEMIS is observing simultaneously at infrared and visible wavelengths, which is not
583 always the case, due to other mission requirements. Although events will be rare, such
584 searches may be still be fruitful, as the combination of the simultaneous observation by
585 THEMIS of visible, infrared spectral and infrared temperature data provides unique
586 opportunity to explore martian dust devil properties, by comparing lofted dust loading
587 and dust temperature with surface conditions.

588 ## *Acknowledgements*

589 Matt Balme is thanked for useful discussions. Martin Towner is funded in part by
590 the UK Science and Technology Funding Council, UK. Two anonymous reviewers are
591 thanked for their detailed work, which greatly enhanced the quality of this paper.

592 ## *References*

593

594 Baddeley, P. F. H. (1860), *Whirlwinds and dust storms of India*, Bell and Daldy, London.

595 Balme, M. R., S. M. Metzger, M. C. Towner, T. J. Ringrose, R. Greeley, and J. D.
596 Iversen (2003a), Frictions wind speeds in dust devils: a field study, *Geophys. Res. Lett.*,
597 *30*(16), 1830, DOI 1810.1029/2003GL017493.

598 Balme, M. R., P. L. Whelley, and R. Greeley (2003b), Mars: dust devil track survey in
599 Argyre Planitia and Hellas Basin, *J. Geophys. Res.*, *108*(E8), doi:10.1029/2003JE002096.

600 Balme, M. R., and R. Greeley (2006), Dust devils on Earth and Mars, *Rev. Geophysics*,
601 *44*(RG3003), doi:10.1029/2005RG000188.

602 Balme, M. R., and A. Hagermann (2006), Particle lifting at the soil-air interface by
603 atmospheric pressure excursions in dust devils, *Geophys. Res. Lett.*, *33*(L19S01),
604 doi:10.1029/2006GL026819.

605 Bell, F. (1967), Dust devils and aviation, Meteorol. Note 27, Aust. Bur. of Meteorol.,
606 Melbourne, Victoria.

607 Biener, K. K., P. E. Geissler, A. S. McEwen, and C. B. Leovy (2002), Observations of
608 martian dust devils in MOC wide angle camera images, paper presented at 33rd Lunar
609 and Planetary Science Conference, Houston, Texas, USA.

610 Briggs, G. A., W. A. Baum, and J. Barnes (1979), Viking Orbiter Imaging Observations
611 of Dust in the Martian Atmosphere, *J. Geophys. Res.*, *84*(B6), 2795-2820.

612 Brumby, S. P., D. T. Vaniman, and D. Bish (2003), Emissivity spectrum of a large "dark
613 streak" from THEMIS infrared imagery, paper presented at Sixth International
614 Conference on Mars, Lunar and Planetary Institute, Pasadena, USA.

615 Cantor, B. A., P. B. James, M. Caplinger, and M. J. Wolff (2001), Martian Dust Storms:
616 1999 Mars Orbiter Camera observations, *J. Geophys. Res.*, *106*(E10), 23653-23687.

617 Cantor, B. A., and K. S. Edgett (2002), Martian Dust Devils: 2 Mars Years of MGS MOC
618 Observations, *AGU Fall Meeting Abstracts*, *51*, 0331.

619 Cantor, B. A., M. C. Malin, and K. S. Edgett (2002), Multiyear Mars Orbital Camera
620 (MOC) observations of repeated martian weather phenomena during the northern summer
621 season, *J. Geophys. Res.*, *107*(E3), doi:10.1029/2001JE001588.

622 Cantor, B. A., K. M. Kanak, and K. S. Edgett (2006), MOC observations of martian dust
623 devils and their tracks (September 1997 – January 2006) and evaluation of theoretical
624 vortex models, *J. Geophys. Res.*, *111*(E12002), doi:10.1029/2006JE002700.

625 Christensen, P. R., B. M. Jakosky, H. H. Kieffer, M. C. Malin, H. Y. McSween Jr., K.
626 Nealson, G. L. Mehall, S. H. Silverman, S. Ferry, M. Caplinger, and M. Ravine (2004),
627 The Thermal Emission Imaging System (THEMIS) for the Mars 2001 Odyssey Mission,
628 *Space Science Reviews*, *110*(1-2), 85-130.

629 Church, C. R., J. T. Snow, G. L. Baker, and E. M. Agee (1979), Characteristics of
630 tornado-like vortices as a function of swirl ratio: A laboratory investigation, *J.*
631 *Atmospheric Sciences*, *36*, 1755-1776.

632 Cooley, J. R. (1971), Dust devil meteorology, NOAA Tech memo NWS CR-42.

633 Cushing, G. E., T. N. Titus, and P. R. Christensen (2005), THEMIS VIS and IR
634 observations of a high-altitude martian dust devil, *Geophys. Res. Lett.*, *32*(L23202),
635 doi:10.1029/2005GL024478.

636 Edgett, K. S., and M. C. Malin (2000), Martian dust streaks and surface albedo controls:
637 thin, dark (and sometimes bright) streaks and dust devils in MGS MOC high resolution
638 pictures, paper presented at 32nd Lunar Planet. Sci., Houston, Texas, USA.

639 Ferri, F., P. G. Smith, M. T. Lemmon, and N. O. Renno (2003), Dust devils as observed
640 by Mars Pathfinder, *J. Geophys. Res.*, *108*(E12), doi:10.1029/2000JE001421.

641 Fisher, J. A., M. I. Richardson, C. E. Newman, M. A. Szwast, C. Graf, S. Basu, S. P.
642 Ewald, A. D. Toigo, and R. J. Wilson (2005), A survey of martian dust devil activity
643 using Mars Global Surveyor Mars Orbiter Camera images, *J. Geophys. Res.*,
644 *110*(E03004), doi:10.1029/2003JE002165.

645 Fitzjarrald, D. E. (1972), The dust devil: a laboratory and field investigation, PhD thesis,
646 186 pp, University of California, Los Angeles.

647 Fitzjarrald, D. E. (1973), A field investigation of dust devils, *J. App. Meteorology*, *12*,
648 808-813.

649 Flower, W. D. (1936), Sand devils, *Prof. Notes. Met. Office*, *71*(5).

650 Fuerstenau, S. D. (2006), Solar heating of suspended particles and the dynamics of
651 martian dust devils, *Geophys. Res. Lett.*, *33*(L19S03), doi:10.1029/2006GL026798.

652 Grant, C. G. (1949), Dust-devils in the sub-arctic, *Weather*, *4*, 402-403.

653 Greeley, R., and J. D. Iversen (1985), *Wind as a Geological Process on Earth, Mars,*
654 *Venus and Titan*, Cambridge University Press, Cambridge.

655 Greeley, R., M. R. Balme, J. D. Iversen, S. M. Metzger, R. Mickelson, J. Phoreman, and
656 B. R. White (2003), Martian dust devils: Laboratory simulations of particle threshold, *J.*
657 *Geophys. Res.*, *108*(E5), 5041, doi:5010.1029/2002JE001987.

658 Greeley, R., S. W. Squyres, R. Arvidson, P. Bartlett, J. B. Bell, D. Blaney, N. A. Cabrol,
659 J. Farmer, B. Farrand, M. P. Golombek, S. P. Gorevan, J. A. Grant, A. F. C. Haldemann,
660 K. E. Herkenhoff, J. Johnson, G. A. Landis, M. B. Madsen, S. M. McLennon, J. Moersch,
661 J. W. Rice, L. Richter, S. Ruff, R. J. Sullivan, S. D. Thompson, A. Wang, C. M. Weitz, P.
662 L. Whelley, and A. S. Team (2004), Wind-related processes detected by the Spirit rover
663 at Gusev crater, Mars, *Science*, *305*, 810-821.

664 Greeley, R., P. L. Whelley, R. E. Arvidson, N. A. Cabrol, D. J. Foley, B. J. Franklin, P.
665 E. Geissler, M. P. Golombek, R. O. Kuzmin, G. A. Landis, M. T. Lemmon, L. D. V.
666 Neakrase, S. W. Squyres, and S. D. Thompson (2006), Active dust devils in Gusev crater,
667 Mars: Observations from the Mars Exploration Rover Spirit, *J. Geophys. Res.*,
668 *111*(E12S09), doi:10.1029/2006JE002743.

669 Hess, G. D., and K. T. Spillane (1990), Characteristics of dust devils in Australia, *J. App.*
670 *Meteorology*, *29*, 499-507.

671 Ives, R., L. (1947), Behavior of dust devils, *Bull. Am. Meteorol. Soc.*, *28*, 168-174.

672 Kaimal, J. C., and J. A. Businger (1970), Case studies of a convective plume and a dust
673 devil, *J. App. Meteorology*, *9*, 612-621.

674 Landis, G. A. (1996), Dust obscuration of Mars solar arrays, *Acta Astronautica*, *38*(11),
675 885-891.

676 Lorenz, R. D. (2004), Thermal imaging of a desert dust devil, *Journal of Meteorology*,
677 *29*(292), 275-276.

678 Malin, M. C., and K. S. Edgett (2001), Mars Global Surveyor Mars Orbiter Camera:
679 Interplanetary cruise through primary mission *J. Geophys. Res.*, *106*(E10), 23429-23570.

680 Metzger, S. M., J. R. Carr, J. B. Johnson, T. J. Parker, and M. T. Lemmon (1999), Dust
681 devil vortices as seen by the Mars Pathfinder camera, *Geophys. Res. Lett.*, *26*(18), 2781-
682 2784.

683 Mullen, J. B., and T. Maxworthy (1977), A laboratory model of dust devil vortices,
684 *Dynamics of Atmospheres and Oceans*, *1*, 181-214.

685 Murphy, J. R., and S. Nelli (2002), Mars Pathfinder convective vortices: frequency of
686 occurence, *Geophys. Res. Lett.*, *29*(23), 18.

687 Ockert-Bell, M. E., J. F. Bell, J. B. Pollack, C. P. McKay, and F. Forget (1997),
688 Absorption and scattering properties of the martian dust, *J. Geophys. Res.*, *102*(E4),
689 9039-9050.

690 Renno, N. O., M. L. Burkett, and M. P. Larkin (1998), A simple thermodynamical theory
691 for dust devils, *J. Atmospheric Sciences*, *55*, 3244-3252.

692 Renno, N. O., A. A. Nash, J. I. Lunine, and J. R. Murphy (2000), Martian and terrestrial
693 dust devils: test of a scaling theory using Pathfinder data, *J. Geophys. Res.*, *105*(E1),
694 1859-1865.

695 Ringrose, T. J., M. C. Towner, and J. C. Zarnecki (2003), Convective vortices on Mars: A
696 reanalysis of Viking Lander 2 meteorological data, sols 1-60, *Icarus*, *163*(1), 78-87.

697 Roberts-Austen, W. C., and A. W. Rücker (1891), On the specific heat of basalt, *Phil.*
698 *Mag.*, *32*, 353-355.

699 Ryan, J. A., and J. J. Carroll (1970), Dust devil velocities: mature state, *J. Geophys. Res.*,
700 *75*(3), 531-541.

701 Ryan, J. A. (1972), Relation of dust devil frequency and diameter to atmospheric
702 temperature, *J. Geophys. Res.*, *77*(36), 7133-7137.

703 Ryan, J. A., and R. D. Lucich (1983), Possible dust devil vortices on Mars, *J. Geophys.*
704 *Res.*, *88*(C15), 11005-11011.

705 Sinclair, P. C. (1964), Some preliminary dust devil measurements, *Monthly Weather*
706 *Review*, *92*(8), 363-367.

707 Sinclair, P. C. (1966), A quantitative analysis of the dust devil, PhD thesis, 292 pp,
708 University of Arizona.

709 Sinclair, P. C. (1969), General characteristics of dust devils, *J. App. Meteorology*, *8*, 32-
710 45.

711 Sinclair, P. C. (1973), The lower structure of dust devils, *J. Atmospheric Sciences*, *30*,
712 1599-1619.

713 Smith, M. D., J. C. Pearl, B. J. Conrath, and P. R. Christensen (2000), Mars Global
714 Surveyor TES observations of dust opacity during aerobraking and science phasing, *J.*
715 *Geophys. Res.*, *105*(E4), 9539-9552.

716 Smith, M. D., J. L. Bandfield, P. R. Christensen, and M. I. Richardson (2003), Thermal
717 Emission Imaging System (THEMIS) infrared observations of atmospheric dust and
718 water ice cloud optical depth, *J. Geophys. Res.*, *108*(E11), 5115.

719 Snow, J. T. (1987), Atmospheric columnar vortices, *Reviews of Geophysics*, *25*(3), 371-
720 385.

721 Stanzel, C., M. Patzold, R. Greeley, and E. Hauber (2006), Dust devils on Mars observed
722 by the High Resolution Stereo Camera, *Geophys. Res. Lett.*, *33*(L11202),
723 doi:10.1029/2006GL025816.

724 Stanzel, C., M. Patzold, D. A. Williams, P. L. Whelley, R. Greeley, G. Neukum, and E.
725 al. (2008), Dust devil speeds, directions of motion and general characteristics observed by
726 the Mars Express High Resolution Stereo Camera, *Icarus*, *197*, 39-51.

727 Thomas, P. C., and P. J. Gierasch (1985), Dust devils on Mars, *Science*, *230*(4722), 175-
728 177.

729 Tomasko, M., L. R. Doose, M. T. Lemmon, P. H. Smith, and E. Wegryn (1999),
730 Properties of dust in the martian atmosphere from the imager on Mars Pathfinder, *J.*
731 *Geophys. Res.*, *104*(E4), 8987-9007.

732 Tratt, D. M., M. H. Hecht, D. C. Catling, and E. C. Samulon (2003), In situ measurement
733 of dust devil dynamics: Toward a strategy for Mars, *J. Geophys. Res.*, *108*(E11), 5116.

734 Whelley, P. L., and R. Greeley (2006), Latitudinal dependency in dust devil activity on
735 Mars, *J. Geophys. Res.*, *111*(E10003), doi:10.1029/2006JE002677.
736
737

738 ## *Figure Captions*

739

740 **Figure 1 – A plot of dust devil positions, with MOLA shaded relief as a background. Symbols**
741 **indicate the positions of dust devils observed, while the symbol labels refer to the dust devil number**
742 **in Table 1 and the text.**

743

744 **Figure 2 – Left-hand images show the THEMIS visible-wavelength scenes of dust devils, on the**
745 **right are THEMIS IR temperature variations (overlain by visible-wavelength intensity contours**
746 **derived from concurrent observations). In all images, Sun illumination is from the left, about 280-300**
747 **azimuth. (North is to the top). The scale bars are 1 km long. Absolute temperature varies from scene**
748 **to scene, but in all cases the red-blue corresponds to a 3K temperature difference. (a) V02114009**
749 **(dust devil 1 in Table 1), (b) V02326010 (dust devil 2), (c) V02326010 (dust devil 3), (d) V02502006**
750 **(dust devil 4), (e) V03334003 (dust devil 5), (f) V03334003 (dust devil 6), (g) V03343003 (dust devil 7),**
751 **(h) V02326010 (dust devil 8)**

752

753 **Figure 3 – Two examples of dust devil candidates that were not confirmed as definite. (a)**
754 **Shows a low resolution dust devil candidate, with no other supporting coverage (THEMIS image**
755 **V09950014). (b) Indicates a possible candidate obscured by the saturation of the image (THEMIS**
756 **images V03343003 and V07837020). The scale bars are 1 km.**

757

758 **Figure 4 – Examples of terrestrial dust devils, ranging from well structured to more**
759 **disordered. (a) shows the classic dust devil structure with a dust column made up of fine suspended**
760 **particles and a slightly wider saltation skirt near the surface. (b) has a weaker structure, and lower**
761 **dust loading, but is physically larger in diameter.**

762

763 **Figure 5 – The illumination geometry for dust devil imagery. θ is the solar incidence angle. I_{src}**
764 **is solar illumination. R_s and R_{dd} are the radiances detected by the spacecraft from the unobstructed**
765 **surface and of the dust devil's shadow respectively.**
766
767

Tables

	Image	Image resolution (m/pixel)	Latitude (N)	Longitude (E)	Height (±50 m)	Diameter (m)	Altitude (m)[b]	Date (yyyy-mm-dd)	L_s	Local time	Correlating images
1	V02114009	36	26°24'10.4"	231°56'11.5"	1500	335	-812	2002-06-06	23.6	15:47	V13697011, 3115_0000[d]
2	V02326010	36	34°26'19.7"	239°22'48.0"	1900	170	2252	2002-06-24	31.6	15:58	1576_0009[d], 1316_0000[d]
3	V02326010	36	35°25'1.7"	239°41'23.6"	>1700[a]	260	2252	2002-06-24	31.6	15:58	1576_0009[d], 1587_0009[d]
4	V02502006	36	35°15'73.0"	203°40'46.1"	550	230	-3951	2002-07-08	38.2	16:05	P01_001393_2161_XN_36N156W[e]
5	V03334003	72	24°51'20.3"	327°53'56.9"	?[c]	310	-3655	2002-09-15	68.4	16:29	V05244026
6	V03334003	72	24°38'43.3"	327°40'54.2"	?[c]	240	-3655	2002-09-15	68.4	16:29	V14717013
7	V03343003	72	6°58'46.3"	65°44'31.4"	250	225	1986	2002-09-15	68.8	16:24	V14414019
8	V02326010	36	36°12'27.6"	120°23'44.1"	350	110	2384	2002-06-24	31.6	15:58	V20336003

Table 1 – The results of dust devil survey. Dust devil height is inferred from shadow length and solar illumination angle. An estimate the accuracy in the diameter is given by the image resolution column.

[a], minimum size is constrained by shadow impinging on the edge of the image, but maximum unknown. [b], is relative to Mars datum. [c], there is no clear shadow seen. [d], image from Mars Express HRSC. [e], image from Mars Reconnaissance Orbiter CTX.

Image	Latitude (N)	Longitude (E)	Ls	Local time	Comments
V01770009	17°5'38.4"	71°30'7.2"	10.2	15:32	Too small to resolve clearly in THEMIS visible, no other coverage
V02055003	11°26'16.8"	131°20'56.4"	21.3	15:41	Too small to resolve clearly in THEMIS visible, no other coverage
V10398001	-9°19'33.6"	21°46'8.4"	21.2	16:29	Structure unclear due to surface features, other coverage lower resolution
V10259008	7°45'21.6"	44°52'58.8"	15.8	16:28	Too small to resolve clearly in THEMIS visible, no other coverage
V18471001	-4°16'55.2"	61°19'55.2"	10.6	16:26	Structure unclear due to surface features, no other coverage
V03014004	3°49'15.6"	193°37'40.8"	56.9	16:14	Bright spot but lack structure, interfering surface features, no other coverage
V02498007	25°23'9.6"	317°31'55.2"	38	16:01	Too small to resolve clearly in THEMIS visible, no other coverage
V09950014	17°16'33.6"	319°44'49.2"	3.5	16:22	Too small to resolve clearly in THEMIS visible, no other coverage
V03343003	6°13'28"	65°47'60.0"	68.8	16:24	Possible small dust devil, signal to noise too low to resolve clearly, no better coverage
V18311007	3°15'0"	328°57'39.6"	4.2	16:23	Bright spot but lack of dust devil structure, no other coverage

Table 2 – Discarded dust devil candidates, with a brief description of the reason for discard. Latitude and longitude refers to the image location. Two examples of these are shown in Figure 3.

Time of Day	No. of dust devils	No. of THEMIS images	Total area imaged (km^2)	Rate of occurrence ($km^{-2}hr^{-1}$)
Before 15:00	0	0	0	
15:00-15:30	0	211	219000	$< 1.82x10^{-5}$
15:30-15:45	0	321	536000	$< 7.45x10^{-6}$
15:45-16:00	4	287	533000	$3.00x10^{-5}$
16:00-16:15	1	242	526000	$7.60x10^{-6}$
16:15-16:30	3	2018	2609000	$4.61x10^{-6}$

Table 3 – A summary of detected dust devil survey statistics.

	THEMIS image	Compensation image	*r*	R_{dd}	R_s	R_T	Plume Opacity	Incidence angle	Dust load (kgm^{-3})
1	V02114009	V13697011	0.998	169.4	177.5	38.0	0.0594	55.8	$1.94x10^{-5}$
2	V02326010	H1316_0000	0.995	119	138.7	46.0	0.2436	57.8	$1.53x10^{-4}$
3	V02326010	H1576_0009	0.971	134.7	139.5	46.0	0.0823	57.8	$3.39x10^{-5}$
4	V02502006	[a]		174.4	209.8	43.0	0.2384	58.1	$1.14x10^{-4}$
5	V03334003	H1619_0000		No shadow	No shadow			60.6	
6	V03334003	V05244026		No shadow	No shadow			60.6	
7	V03343003	V14414019	0.975	142.3	154.5	12.0	0.1083	65.8	$4.78x10^{-5}$
8	V02326010	V20336003	0.990	125.5	135.8	46.0	0.1317	57.8	$1.28x10^{-4}$

Table 4 – Opacity and dust loading estimates for confirmed dust devils. HRSC images are indicated by starting with H, while THEMIS images start with V. Dust devils 5 and 6 do not appear to have a significant shadow, as discussed further in text. [a] indicates that no THEMIS or HRSC compensation images exist, and *r* is assumed to be 1. The radiance values R_{dd}, R_s and R_T are byte scaled.

Fig 1

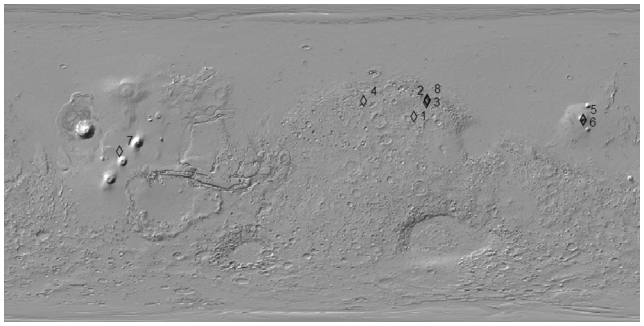

Fig 2

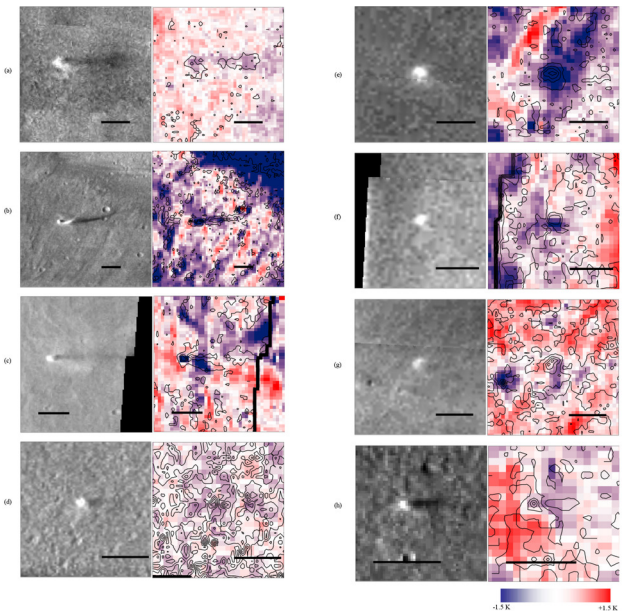

Fig 3

(a)

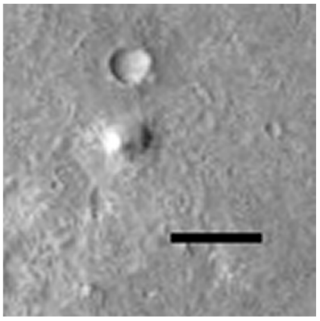

(b)

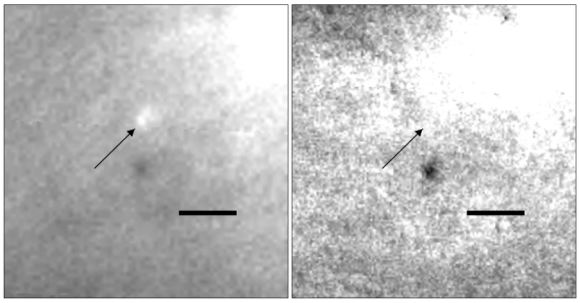

Fig 4

(a) (b)

Fig 5